Insights from modeling metabolism and amoeboid cell motility in the immune system

Steijn, L. van

Chapter 4

Topotaxis on silicon and *in silico*: Obstacle-induced contact-inihibition of locomotion explains topotactic cell navigation in dense microenvironments

Leonie van Steijn, Joeri A.J. Wondergem, Koen Schakenraad, Doris Heinrich, Roeland M.H. Merks

Abstract

During biological development, cancer metastasis and in the immune system, cells navigate through dense environments filled with obstacles such as other cells and the extracellular matrix. Recently, the term 'topotaxis' has been introduced for the navigation of cells along topographic cues such as density gradients of obstacles. Experimental and mathematical efforts have analysed topotaxis by looking at the migration of single cells in pillared grids, in which topographic gradients can be defined precisely as a pillar density gradient. We have previously introduced a model based on active Brownian particles (ABP) which has shown that ABPs perform topotaxis, i.e., drift, on average, to lower pillar densities, due to the decrease in effective persistence time when pillars are closer together. Whereas topotactic drifts of up to 5% of the instantaneous cell speed have been observed experimentally, the ABP model could only predict topotactic drifts of up to 1%. We hypothesized that the discrepancy between the ABP and the experimental observations is in 1) the deformable cell volume, and 2) the cell-pillar interactions. Here we introduce a more detailed model of topotaxis, based on the Cellular Potts model. To model persistent cells we use two methods: the Act model by Niculescu et al., and a method similar to the ABP model. After fitting our model parameters to yield the same motion as experimentally found for *D. discoideum* on an empty field, we study how topotaxis is performed. For starved *D. discoideum*, our model predictions are close to the experimental results, especially when we correct for the fact that our simulated cells have a higher speed. However,

topotactic efficiency is different between the two persistence methods, with the Act model outperforming the ABP persistent model. We found that the Act model shows a larger reduction in effective persistence time in pillar grids than the vector model. Lastly, we also modeled the slow and less persistent vegetative *D. discoideum* cells, for which our model predicted a small topotaxis drift. Here, both model variants predicted similar topotaxis, contrasting with the starved cell results.

Popular summary

Cell motility is an important function in development and immunity. Knowing how the environment influence cell motility is useful in developing methods to interfere during disease or in tissue engineering. One of the ways the environment affects cell motility is by the presence of obstacles. Previous work has shown that single cells move from a high density of obstacles to a lower density of obstacles, a process called topotaxis. A previous mathematical model, modelling cells as particles showed that the velocity at which cells move from high to low obstacle density, the topotactic drift, can in part be explained by reduced persistence: i.e. the closer the obstacles are together, the quicker the particle looses its direction, resulting in a bias towards less obstacle dense areas. However, the experimentally found topotactic drift was higher.

In this work, we look at cell motility in obstacle gradients with a more realistic cell model with deformable cells and compare those to an experimental setup. We used two different methods to model the persistence of cells: one which models the cytoskeleton and with active reorientation after collisions, the other similar to the previous mathematical model and with passive reorientation after collisions. We fitted our model to experimental cell motion. Both models as well as the experiments show more topotactic drift in steeper obstacle gradients. The model with active reorientation shows a better match in topotaxis efficiency and outperforms the model with passive reorientation. This is due to a larger loss of persistence when collisions feed back to cell motility.

Next steps would be to investigate more complex environments. Interesting directions would be the integration of multiple environmental cues, such as chemotaxis, in the model, and exploration of how obstacle shape influences topotaxis, so that we get a better understanding of cell navigation in the body.

4.1 Introduction

Motile cells within the body encounter many obstacles such as other cells and extracellular matrix, as they move through a tissue. How cells react to the density of obstacles is of importance for many processes, such as cancer cells invading from a dense tumor into looser packed tissues [180, 181], immune cells moving through tissues with different porosity [182, 183] or pathogens such as *Plasmodium* that migrate through different tissue throughout their life cycle [184, 185]. It has been shown that cell can use the topography of the environment as a way to orient themselves [186, 187, 188]. So far, topotaxis has only been shown in *in vitro* environments, but it will also likely play a role in *in vivo* systems.

To study topotaxis quantitatively, a collection of *in vitro* models have been developed to provide well-defined topographic cues to migrating cells. In [186], cells are allowed to move on a subcellular-patterned array coated with fibronectin. Cells follow the gradient in nanopattern, from dense to sparser patterning. In [187], cells were put on polyurethane acrylate nanohairs. These hairs were either vertical, or bent in a specific direction. Cells on top of these hairs moved with a bias towards the bent direction, but without bias on straight hairs. Also larger scale cues are known: in [188], cells were placed on micropatterned substrates. The patterns were either disconnected cell-sized triangles in a line, connected cell-sized triangles in a line and a belt. They showed that cells in disconnected triangles hardly moved from one spot to another, whereas cells in the other two patterns did. Cells in the belt moved without preferential direction over the belt, but the cells on the connected triangles moved with a bias in the direction of the triangles. The rearrangement of actin and formation of the lamellipodium were key players in this bias or ratcheting. An extensive review of other cues in 'ratchettaxis' has been done in [189].

Wondergem et al. showed another setup in which topotaxis arises from a cell-size cue [74]. They let starved *Dictyostelium discoideum* cells move on a grid with micropillars placed with increasing pillar spacing in one direction. As in previous work with isotropic pillar lattices [190][191], the size of these micropillars were in the order of *Dictyostelium* cell size, in contrast to [186] and many of the structures described in [189]. They found that, on average, cells move to the side with larger pillar distance, with a velocity of about 5% of their instantaneous speed.

Because *Dictyostelium* cells are persistent walkers [192], we hypothesized that pillars alter this persistent motion. Once a cell bumps into a pillar, it cannot continue and will have to change its direction, and hence change its persistence. This first hypothesis on this form of topotaxis was tested

by Schakenraad et al. [75]. They tested whether this topotaxis could be explained by altered persistence lengths, similar to durotaxis on a stiffness gradient [193] where cells on softer substrates change direction more often than on stiffer substrates, or bacterial chemotaxis [194] where cells perform more tumbles in lower concentration of the chemoattractant. Using a model with Active Brownian Particles, which also perform persistent motion, Schakenraad et al. showed that indeed topotaxis can be derived from altered persistence lengths due to pillar spacing. However, the ABP model could explain only a topotaxis of 1% of the intrinsic cell speed, significantly lower than the 5% found in *Dictyostelium* experiments. Here we propose a refined model for topotaxis giving a better match with the experiments.

This previous work shows that topotaxis in gradient pillar density can partially be explained by changed effective persistence lengths. However, what are the remaining factors that can explain the gap in topotactic drift between ABPs and *Dictyostelium* cells? Some candidates are easy to point out: ABPs are point-particles, whereas cells have a deformable and non-zero volume. We can therefore expect cells to have a minimum pillar distance through which they can move, as well as larger than zero area of interaction between the cells and pillars. This cell-pillar interaction points to another candidate: how cells reorient after collision. Where ABPs only change their target direction by thermal fluctuation, cells can actively reorient themselves. A well studied example of cell reorientation is Contact Inhibition of Locomotion (CIL), where cells reorient themselves after collision with another cell.

In this work, we model a persistently moving, deformable cell with volume using the Cellular Potts model and test two different schemes for cell persistence. The first scheme used the Act model which models internal cell skeleton rearrangements [73]. This allows for emergent, active reorientation as the cell cannot extend further into a pillar and will polarize elsewhere, similar to CIL. As a control, the second scheme resembles the ABP model and shows no CIL, as we explicitly assign a direction to a cell together with a persistence time, which results in passive reorientation upon collision. Before we look into topotaxis, we search for parameter settings that match experimental *Dictyostelium* cells on an empty field so we can quantitatively compare our model results with the experimental results of persistently moving starved and less persistently moving vegetative *Dictyostelium* cells.

For the starved parameter settings, the two different persistence schemes results in different topotaxis, with the active reorientation model having more efficient topotaxis. Our models slightly overpredict topotaxis compared to the experimental results, but the main difference is cell speed,

which is much higher in the simulations than in the experiments. On a relative level, the model topotaxis and experimental topotaxis match very closely, with the active reorientation model being a closer match. Trying to explain the difference in speed, we test the effect of interaction between pillar and cell, by changing the adhesion energy between them. However, when simulated cell speed approximates experimental cell speeds, the cells are largely sticking to the pillars, which we do not observe in the experiments. Finally, we also predict a minute effect of the pillar grid on vegetative *Dictyostelium*, that is only visible for very steep pillar gradients, and is independent of persistence scheme.

4.2 Results

We characterized topotaxis for *in vitro* starved *D. discoideum* cells, and developed a Cellular Potts model with persistent cell motion with active or passive reorientation upon collisions. Before we compared topotaxis measured in experiments and topotaxis measured in simulations, we made sure to match the motility of simulated cells to *in vitro* starved cells. Futhermore, we also matched the motility of simulated cells to *in vitro* vegetative *D. discoideum* cells. After that, we characterized topotaxis in our starved as well as vegetative simulations.

4.2.1 Model

We used the Cellular Potts model to simulate *Dictyostelium discoideum* cells. The Cellular Potts model is a 2D lattice based model in which a cell is represented by a number of lattice sites. The lattice is updated per site, allowing for deformable cells, and a set number of lattice updates is called a Monte Carlo Step (MCS), the time unit we use in this model. We can set a goal cell area and cell perimeter, so we can control cell size and shape to a desired extent.

In order to obtain persistent cell motion, we used two extensions of the CPM. The first, the Act-model, is based on an actin-inspired feedback mechanism that results in cell polarization [73]. It is controlled by two parameters: λ_{Act}, which determines the weight of the Act-model and can also be interpreted as the maximum protrusive force of the actin network, and $\max_{\mathrm{Act}}$, the maximum activity value, also interpretable as the lifetime of an actin subunit within the actin network. By altering these two parameters, a large variety of persistent random walkers can be achieved in this model. Furthermore, due to the feedback mechanism, the cell can loose

its polarization upon collision and repolarize in a different direction, i.e. it has contact inhibition of locomotion. We indicate this model as the active reorientation model.

The second extension is based on the previous ABP model and has a directional vector at its center. The cell is more likely to move in a certain direction if that movement aligns with the directional vector. The directional vector changes over time by a scaled random noise term. This extension is also controlled by two parameters: $\lambda_{\text{persistence}}$, which determines the weight of this extension and how strictly cells should align to their directional vector, and τ, the persistence time of the directional vector. Combinations of these two parameters result in a large variety of persistent random walkers as well. Notably, this model extension has no CIL as the cell will only reorient once its directional vector has changed. We will further indicate this model version as the passive reorientation model.

4.2.2 Matching model parameters to cell motion

In order to match *in silico* cell motility to *in vitro* cell motily, we determined a number of *in vitro* cell properties for starved and vegetative *Dictyostelium discoideum* on a flat PDMS substrate (Figs. 4.1, 4.2). We measured the mean cell area (Figs 4.1D,4.2B), mean cell speed (Figs 4.1E,4.2C), cell persistence time (Figs 4.1G,4.2E) and cell diffusion constant (Figs 4.1H,4.2F), see also Table 4.1. In general, starved *D. discoideum* cells are highly motile and perform a persistent walk, whereas vegetative *D. discoideum* cells are less motile and less persistent.

From these properties, cell area and cell speed were used to set the length and time scale in the CPM. With the free parameters λ_{Act} and $\max_{\text{Act}}$ for the active reorientation model, and $\lambda_{\text{persistence}}$ and τ for the passive reorientation model, we used a hillclimbing algorithm to fit the diffusion constant and persistence time of simulated cells to the *in vitro* values in Table 4.1. The resulting best fits for both starved and vegetative cell motilities and both persistence methods are also shown in Table 4.1, and the corresponding model parameter values are shown in Table 4.2. Overall, we have achieved a good match for the starved cells and a reasonable match for the vegetative cells.

4.2.3 Introducing pillar gradients

With the model performing similar motion to the starved and vegetative cells, we introduced a pillar grid with gradient [75]. The pillar gradient is

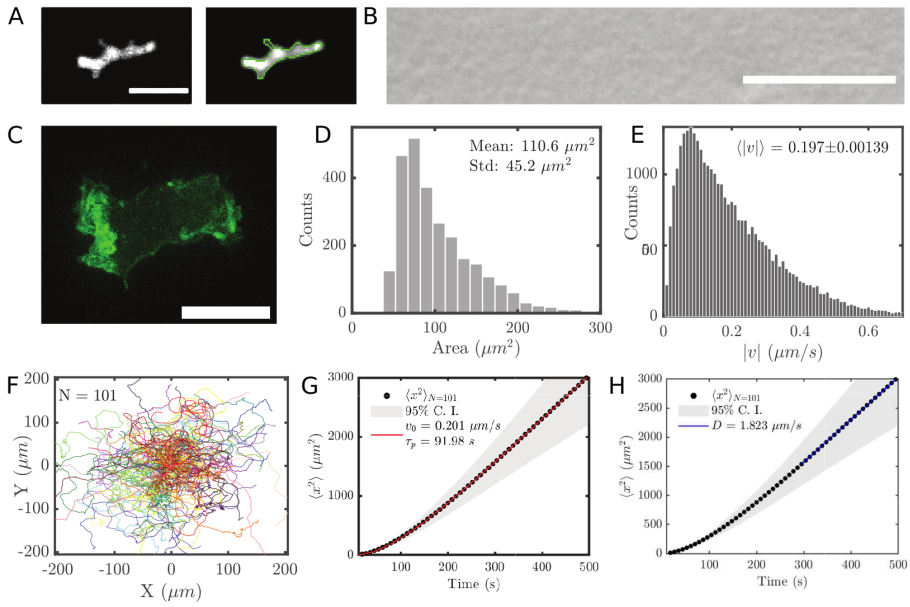

FIGURE 4.1: **Empirical basis of CPM parameter constraints I: starved *D. discoideums***

A) Detection of starved *D. discoideum* motion on flat PDMS was used to calibrate the CPM simulations. Time-lapse fluorescent confocal imaging of cells (left) was used to detect cell edges (green, right). Scale bar is 10 μm. **B)** SEM image of flat PDMS, without engineered topographies the substrate has nanometer scaled features providing traction to cells. Scale bar is 1 μm **C)** Actin polymerization hot spots (visualized through LimE-GFP, z-projection) are highly anisotropically distributed, associated with the high persistence of starved *D. discoideum*. **D)** Areas measured for starved cells on flat PDMS. These determined the area (A_σ) parameter used in the CPM. **E)** Instantaneous velocity distribution of observed cell motility. **F)** Trajectories obtained from live cell imaging. **G)** The MSD (black) of starved *D. discoideum* trajectories is well fit by analytical expression for persistent random particles (red). The average instantaneous velocity ($\langle |v| \rangle$) and persistence time (τ_p) were used to calibrate the vector- and actin based CPMs. **H)** The MSD (black) of starved *D. discoideum* trajectories at larger lag-times is well fit by a line (blue). The slope of the blue line is used to derived the diffusion constant D, which was used to calibrate the vector- and actin based CPMs.

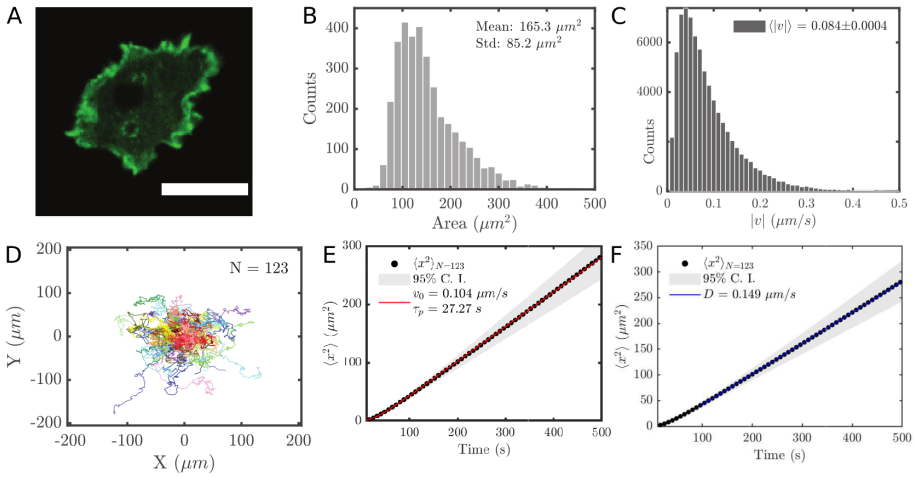

FIGURE 4.2: **Empirical basis of CPM parameter constraints II: vegetative *D. discoideums***

A) Actin polymerization hot spots (visualized through LimE-GFP, z-projection) in the cell are more isotropically distributed in the vegetative state, giving rise to slower and less persistent motion than starved *D. discoideum*. **B)** Areas measured for vegetative cells on flat PDMS. These determined the area (A_σ) parameter used in the CPM. **C)** Instantaneous velocity distribution of observed cell motility. **D)** Trajectories obtained from live cell imaging, motion detection was performed equal to the starved state (see Fig 4.1). **E)** The MSD (black) of starved *D. discoideum* trajectories is well fit by analytical expression for persistent random particles (red, but the parabolic regime for low lag-times is significantly shorter. The average instantaneous velocity ($\langle |v| \rangle$) and persistence time (τ_p) were used to calibrate the vector- and actin based CPMs. **F)** The MSD (black) of starved *D. discoideum* trajectories at larger lag-times is well fit by a line (blue). The slope of the blue line is used to derived the diffusion constant D, which was used to calibrate the vector- and actin based CPMs.

TABLE 4.1: Cell motility properties for the experimental data and best fits for the active and passive reorientation models.

	Starved		
	Experimental	Active	Passive
Length equivalent 1px (μm)	-	0.525	0.525
Time equivalent 1 MCS (s)	-	0.373	0.574
Speed ($\mu m/s$)	0.197±0.001	-	-
Area (μm^2)	110.4±45.1	-	-
Effective diffusion ($\mu m^2/s$)	1.82±0.68	1.76±0.08	1.87±0.08
Persistence time (s)	91.98±0.98	89.30±2.22	89.89±3.33
	Vegetative		
	Experimental	Active	Passive
Length equivalent 1px (μm)	-	0.524	0.524
Time equivalent 1 MCS (s)	-	0.388	0.821
Speed ($\mu m/s$)	0.084±0.0004	-	-
Area (μm^2)	164.6±84.3	-	-
Effective diffusion ($\mu m^2/s$)	$0.149\pm4.89\times10^{-4}$	0.137±0.007	0.121±0.006
Persistence time (s)	27.41±0.41	25.48±0.35	33.27±1.48

TABLE 4.2: Parameters of the best fits for the starved and vegetative *Dictyostelium* cells for both the active and passive reorientation models.

Best fit parameters	Starved	Vegetative
T	20	20
Area	400	600
λ_{area}	50	50
Perimeter	313	350
$\lambda_{perimeter}$	1	1
$J_{cell,medium}$	20	20
Active model		
λ_{Act}	129	80
$\max_{Act}$	37	33
Passive model		
$\lambda_{persistence}$	159	78
τ	30	7

TABLE 4.3: Pillar gradient grid parameter values for the experimental and simulation setup

Parameter	Description	Experiment (µm)	Model (px)	Model (µm)
R	pillar radius	5	10	5.3
h	pillar height	18 ±2	N/A	
d	pillar center distance at origin	16.8	32	16.8
d_{min}	pillar center distance left cap	13.6	26	13.7
d_{max}	pillar center distance right cap	19.9	38	20.0
s	gradient steepness	0.01, 0.03	0.01 - 0.11	

defined according to the set of pillar centers described by

$$P = \left\{ \vec{x} \in \mathbb{R}^2 \;\middle|\; \begin{array}{l} x_1 = \frac{d}{1-e^{-s}}\left(e^{sn}-1\right) + \frac{d}{2} \text{ and} \\ x_2 = d\left(m+\frac{1}{2}\right)e^{sn}, \text{ with } n, m \in \mathbb{Z} \end{array} \right\}.$$

Here, d is the distance between pillar centers at the center of the grid, and s a parameter that controls the steepness of the gradient, with higher s indicating steeper gradients. P defines a pillar gradient in the x-direction with increasing pillar distance from left to right. The gradient is capped a both ends with a regular grid of pillar center distance d_{min} and $d_{max} = 2d - d_{min}$ to prevent cells from not being able to pass in between pillars. All measurements, both for the experimental and simulation setup and including pillar radius and pillar height, are shown in Table 4.3.

In the experimental setup, the pillar grid is a molded PDMS pillar grid. Cells are able to navigate between the pillars and resolve collision with pillars (Fig. 4.3A). Because cells were seeded randomly on the pillar grid, only $s = 0.01$ and $s = 0.03$ were used (Fig. 4.4A,B), as for steeper gradients too few cells are seeded in the short pillar gradients. Starved *D. discoideum* cells were tracked while in the gradient (Fig. 4.4E,F,G).

For the simulations, pillars were modeled as immobile obstacles. Cells could not move into a pillar, but were allowed to retract from them. Adhesion between cell and pillar can be controlled by the contact energy parameter $J_{\text{cell,pillar}}$. We assume that cells show no preference for pillars nor medium, so the contact energies between cell-pillar and cell-medium are equal ($J_{\text{cell,pillar}} = J_{\text{cell,medium}} = 20$), unless stated otherwise. In contrast to the experiments, repeated simulations were done with single cells only, starting from the same initial position in the center of the field, see Figs. 4.5,4.7,4.10.

The different ways in which the two persistence models respond to

obstacles is clarified in Fig. 4.3B,C. For the active reorientation model, we see CIL: once the cell collides with a pillar, it looses its polarization and will repolarize in a different direction from before. For the passive reorientation model, the cell will try to continue into the same direction, even if it is directed into a pillar, until the direction vector is no longer pointing into that pillar. The time it takes to resolve a collision is in the order of minutes, similar to that seen in the experimental setup (Fig. 4.3A).

4.2.4 Starved *D. discoideum* cells show topotactic drift increasing with gradient steepness

In order to measure the effect of topotaxis of starved cells, drift in both the x and y direction (v_x and v_y) was calculated for cell tracks in the gradient (Fig. 4.4F,G,H). More specifically, the migratory drift was calculated by averaging over all x or y displacements of all trajectories. As a control, the migratory drifts were also calculated for starved cells on flat surface. Starved *D. discoideum* cells showed a significant drift in the positive x-direction (i.e. towards lower pillar densities) for both pillar gradients $s = 0.01$ and $s = 0.03$. This holds compared to both the corresponding v_y as well as compared to v_x on flat surface (Fig. 4.4H). Moreover, the cells on the steeper gradient ($s = 0.03$) showed a larger v_x relative to the cells on the $s = 0.01$ gradient.

4.2.5 Reorientation mode of starved cells affects topotactic capacity

We simulated the same gradient pillar grid in our model. Examples of cell tracks and the pillar grids for different gradients are shown in Figure 4.5. Cells move within the pillar grid, but only explore a limited space each. We can see that the active reorientation model on the steep gradient (Fig. 4.5C) does not penetrate into the dense side of the grid as much as the passive reorientation model does (Fig. 4.5F). The population mean x and y coordinates over time (Fig. 4.5G,H) show that there is drift along the x-axis, but not the y-axis, indicating that the simulated cell perform topotaxis in both models.

Figure 4.6A shows the migratory drift in the x-direction (v_x) as a function of s, for the experimentally measured topotaxis (Fig. 4.4H) and both reorientation models for the starved parameter set. The experimental observation of increasing v_x with increasing s in starved cells is also seen in the results of our models (Fig. 4.6A). Both reorientation models extrapolate this trend of v_x increasing with s in a linear fashion. However, there is a

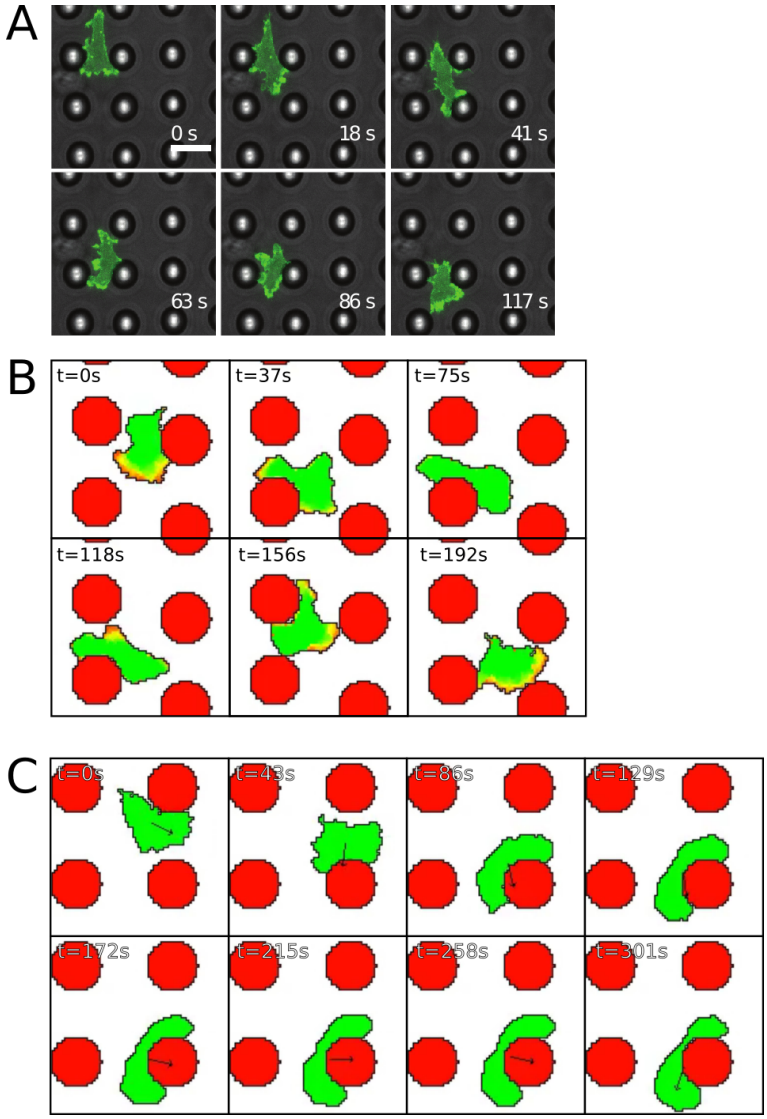

FIGURE 4.3: **Examples of frontal collision of *in vitro* and simulated starved cells with a pillar A)** *in vitro D. discoideum* starved cell in a pillar grid. The arrow indicates qualitatively the direction and magnitude of motion. Cell cytoplasm is labeled fluorescently. **B)** Active reorientation model: Act-levels are colored from red (highest level) to green (Act-level=0). Once the polarized cell hits the pillar, it looses its polarization. A new Act-front appears, the cell polarizes again and moves away from the pillar. **C)** Passive reorientation model simulation: the arrow is the preferential direction vector of the cell, starting at its center of mass. Once the cell collides with the pillar, it can only move away once its directional vector points away from the pillar (final frame).

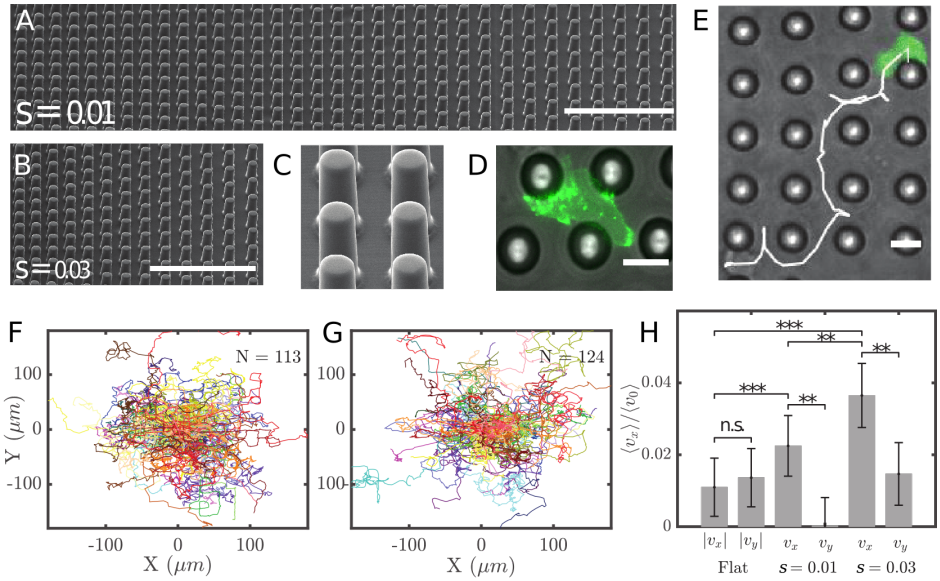

FIGURE 4.4: **Large scale topotaxis for highly-motile amoeboid cell migration (*D. discoideum*) A)** SEM micrograph of the $s = 0.01$ pillar field. Scale bar is 100 μm. **B)** Same micrograph, but for $s = 0.03$. **C)** Detailed micrograph of pillars ($h = 20\mu m$, $d = 10\mu m$). **D)** Actin polymerization hot spots visualized for a cell migrating through a pillar field. Fluorescence is LimE-GFP expressed in LimE null cells [195, 196] after z-projection, scale bar is 10 μm. **E)** Bright field image of a pillar field ($s = 0.03$) overlaid with the trajectory of a migrating starved *D. discoideum* cell (free cytoplasmic GFP in green). Scale bar is 10 μm. **F)** Trajectory plot of cells moving on topotaxis field $s = 0.01$. **G)** Trajectory plot of cells moving on topotaxis field $s = 0.03$. **H)** Drifts ($v_{x,y}$) measured in all live cell experiments (flat, $s = 0.01$ and $s = 0.03$) compared. The anisotropicity in pillar positioning was in the x direction for all non-flat experiments. The topotactic drift (v_x) was found to be significantly higher ($p \leq 0.01$) than noise (v_y) for all topotaxis assays. Additionally, the topotactic drift was found to increase ($p \leq 0.001$) with a rising gradient.

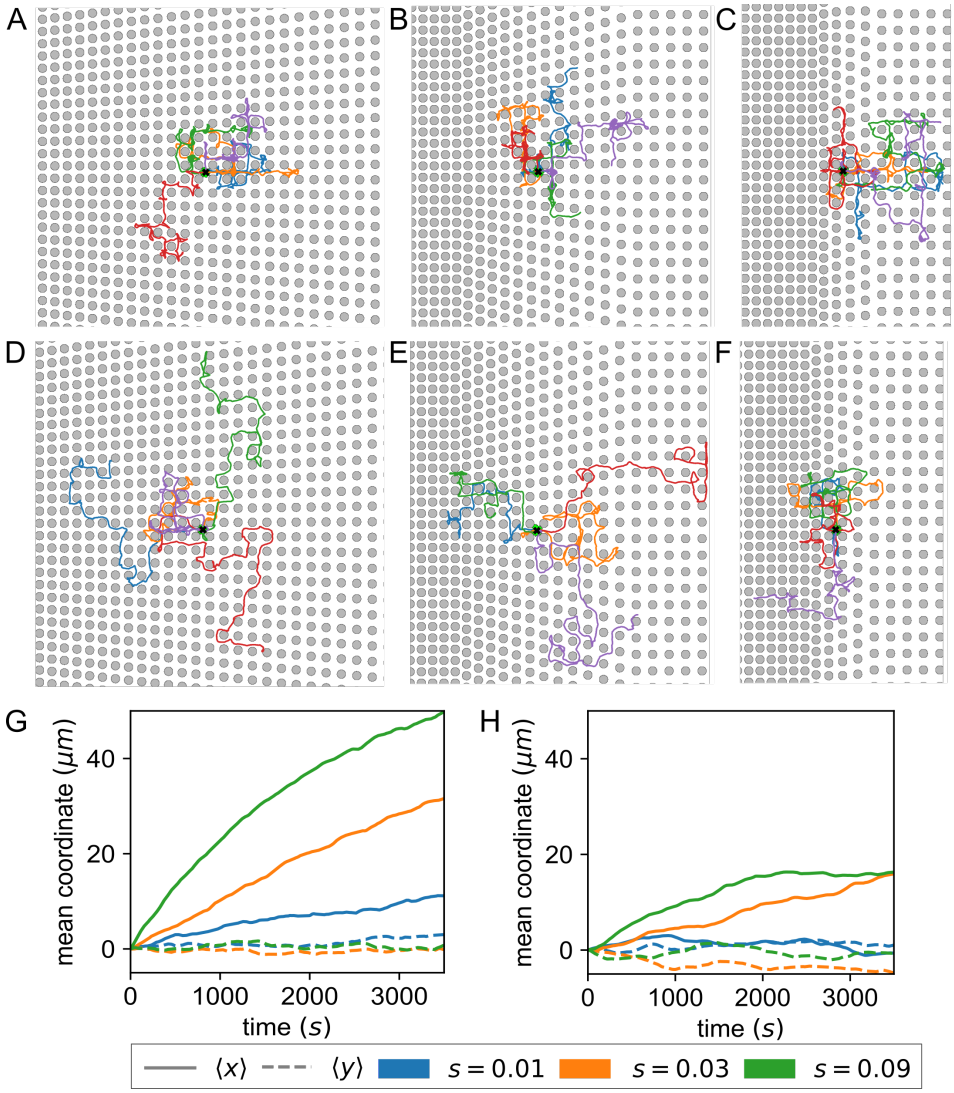

FIGURE 4.5: **Trajectories of starved simulated cells and means of x and y coordinates over time for different gradient steepness parameter (s)-values.** *Top row* active reorientation model example trajectories: **A)** $s = 0.01$, **B)** $s = 0.03$, **C)** $s = 0.09$. *Middle row* passive reorientation model examples: **D)** $s = 0.01$, **E)** $s = 0.03$, **F)** $s = 0.09$. Starting location is marked with a black cross and the depiction of a cell. Each trajectory has its own color. *Bottom row* mean x and y coordinates over time for gradient steepness s corresponding to the gradients shown in the rows above. **G**) Active reorientation model. **H**) Passive reorientation model.

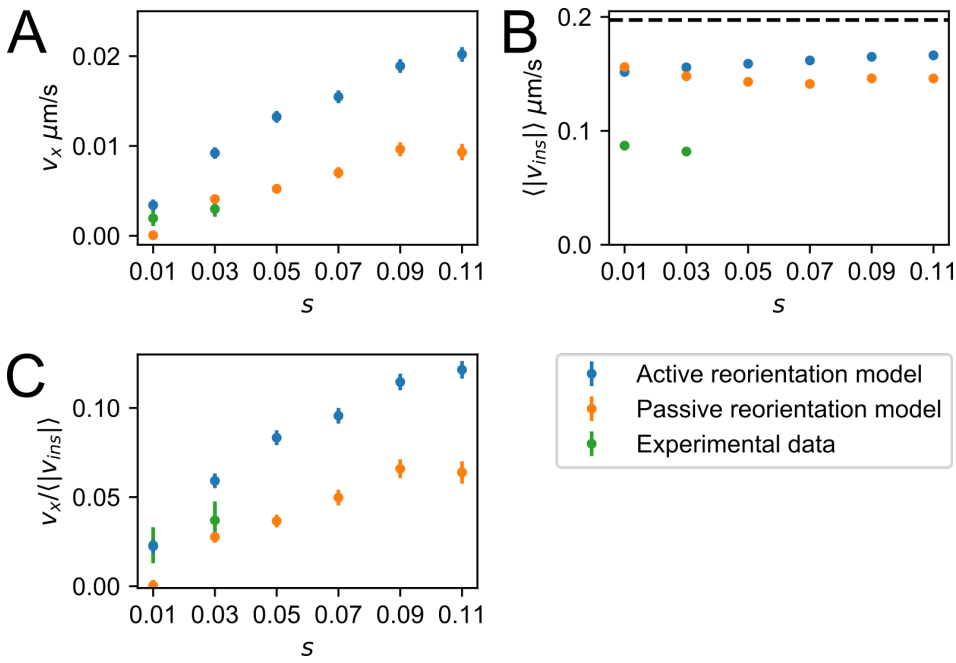

FIGURE 4.6: **Topotactic drift and instantaneous speed of starved parameter set against gradient steepness** s**.** Each orange or blue data point represent the average of a 1000 simulations. Error bars indicate 97.5% CI. **A)** Topotactic drift v_x. **B)** Instantaneous speed $\langle|v_{ins}|\rangle$. Dotted line depicts the instantaneous speed of starved cells in absence of pillars. **C)** Relative topotactic drift $v_x/\langle|v_{ins}|\rangle$).

clear difference in v_x when comparing the two reorientation models: the passive reorientation model shows a lower topotactic drift. Although the fitted parameters of the methods do not result in the exact same persistent random walk, we wouldn't expect such a difference in topotactic drift. Nonetheless, when directly comparing the topotaxis between simulated cells and *D. discoideum* cells, our model predictions are close. For $s = 0.01$, the experimental v_x is in between the active and passive reorientation models' v_x, whereas for $s = 0.03$ both models results in higher v_x, albeit that the passive reorientation model v_x is very close to the experimentally measured v_x.

As Figure 4.3 shows, *Dictyostelium* and simulated cells collide with pillars. This decreases their speed. We measured the mean instantaneous speed $\langle|v_{ins}|\rangle$ of the cells within the pillar grid, shown in Figure 4.6B and Table 4.4. For both experimental and simulated cells, the speed does indeed

TABLE 4.4: Instantaneous speed $\langle|v_{ins}|\rangle$ in $\mu m/s$ on empty field and within pillar grid for starved *D. dictyostelium* cells, starved active reorientation model simulations and starved passive reorientation model simulations. Given error is 97.5% confidence interval.

Field	Experimental	Act based	Vector based
Empty field	0.197±0.00139	0.198±0.00285	0.197±0.001331
$s = 0.01$	0.087±0.00080	0.152±0.00046	0.156±0.000264
$s = 0.03$	0.082±0.00082	0.156±0.00047	0.148±0.000274

drop and is not dependent on pillar gradient steepness s. However, experimental cells show a larger decrease in speed than the simulated cells, about 50% decrease compared to cells on an empty field, versus 20% decrease for the simulated cells. The mean instantaneous speeds of both reorientation models are not far apart.

As our simulated cells move at a higher speed, we would also expect a higher topotactic ddrift. Therefore, aside from comparing absolute topotactic velocities, we also looked at the relative topotactic velocity: $v_x/\langle|v_{ins}|\rangle$, (Fig. 4.6C). For $s = 0.01$, the relative v_x of the experimental data is very similar to that of actively reorienting simulated cells, whereas for $s = 0.03$, the experimental v_x lies between the value of the two reorientation modes, and is closest to the passive reorientation model predictions. We conclude that our models make good prediction for relative topotaxis. Furthermore, the similar mean instantaneous speeds but different topotactic drifts for the active reorientation and passive reorientation model yield different relative topotactic drifts. The active reorientation model's relative topotactic drift is on average twice as large as the passive reorientation model's. This indicates that the persistence method itself causes part of the difference in topotaxis drift, and could be due to CIL in the active reorientation model.

4.2.6 Pillar adhesion changes velocity within the grid

To study what could give rise to the discrepancy between the instantaneous velocity of the experimental and simulated cells, we turned to the interaction between cells and pillars. For the model results in Fig 4.6, we assumed that cells neither adhere to nor are repulsed by the pillar surface, i.e. $J_{\text{cell,medium}} = J_{\text{cell,pillar}}$. However, we can test this assumption and vary the contact energy $J_{\text{cell,pillar}}$. To test whether the adhesiveness of cells to pillars affects topotaxis, we simulated cell movement in a grid with gradient $s = 0.03$ for different contact energies. We let $J_{\text{cell,pillar}}$ range from -60 to 60, where $J_{\text{cell,pillar}} = 20$ is neutral with respect to $J_{\text{cell,medium}} = 20$. Examples

of cell tracks under a subset of this $J_{\text{cell,pillar}}$ range are shown in Fig. 4.7. Clear is that for very low $J_{\text{cell,pillar}}$ (Fig. 4.7A,B,D,E), cell displacement is reduced, and more extremely so for actively reorienting cells than passively reorienting cells. High $J_{\text{cell,pillar}}$ (Fig. 4.7C,F) does not seem to affect cell displacement much compared to neutral $J_{\text{cell,pillar}}$ (Fig. 4.5B,E). A first glance on topotactic drift (Fig. 4.7G,H) shows that the active reorientation model loses it's drift at low $J_{\text{cell,pillar}}$, but not at high $J_{\text{cell,pillar}}$. The passive reorientation model is also affected by pillar adhesiveness, but still displays a drift at low $J_{\text{cell,pillar}}$.

We further quantified the topotactic drift more precisely. Figure 4.8A shows the topotactic drift as a function of $J_{\text{cell,pillar}} - J_{\text{cell,medium}}$ for starved cells. There is an effect of decreasing the adhesion energy $J_{\text{cell,pillar}}$ to negative values, which decreases the topotactic drift. For very negative energy differences, actively reorienting cells eventually do topotaxis in the other direction. However, closer inspection of the cell tracks shows that cells move to the two initial pillars on their left side and get stuck there, see Fig. 4.7A. Increasing $J_{\text{cell,pillar}}$ with respect to $J_{\text{cell,medium}}$ does not seem to have an effect on v_x, suggesting that the topotactic drift saturates with increasing $J_{\text{cell,pillar}}$. Again, we see a difference in the topotactic drift between the two persistence methods (Fig 4.8A).

Aside from collision with pillars, cell-pillar adhesion is now an extra interaction that can influence cell speed. Looking at the $\langle|v_{ins}|\rangle$, we see again differences between the two persistence methods (Fig. 4.8B). For the actively reorienting cells, $\langle|v_{ins}|\rangle$ drops quickly when lowering $J_{\text{cell,pillar}}$, is maximal around $J_{\text{cell,pillar}} = 10$ and slightly decreases for further increase in $J_{\text{cell,pillar}}$. The large drop in $\langle|v_{ins}|\rangle$ confirms the observation on the examples of cell tracks (Fig 4.7A), as cells like to adhere more and more to the pillars and hardly displace. For the passively reorienting cells, $\langle|v_{ins}|\rangle$ doesn't decrease as dramatically as for actively reorienting cells for negative $J_{\text{cell,pillar}}$. Also the optimum in $\langle|v_{ins}|\rangle$ isn't as clear and appears for higher $J_{\text{cell,pillar}} = 20$.

When we compare the results to the experimental data, we can make two observations. First is that the model prediction is close to the v_x of *D. discoideum* cells for $J_{\text{cell,pillar}} - J_{\text{cell,medium}} = -30$. Second is that for $J_{\text{cell,pillar}} - J_{\text{cell,medium}} = -30$, $\langle|v_{ins}|\rangle$ is still higher for the simulated data than the experimental data, resulting in underestimation of the relative topotactic velocity. The values of $J_{\text{cell,pillar}}$ for which the instantaneous speeds are indeed similar between model and experiment are $J_{\text{cell,pillar}} - J_{\text{cell,medium}} = -80$ and -50 for the passive reorientation model and active reorientation model respectively, and are already extreme in limiting cell displacement in general.

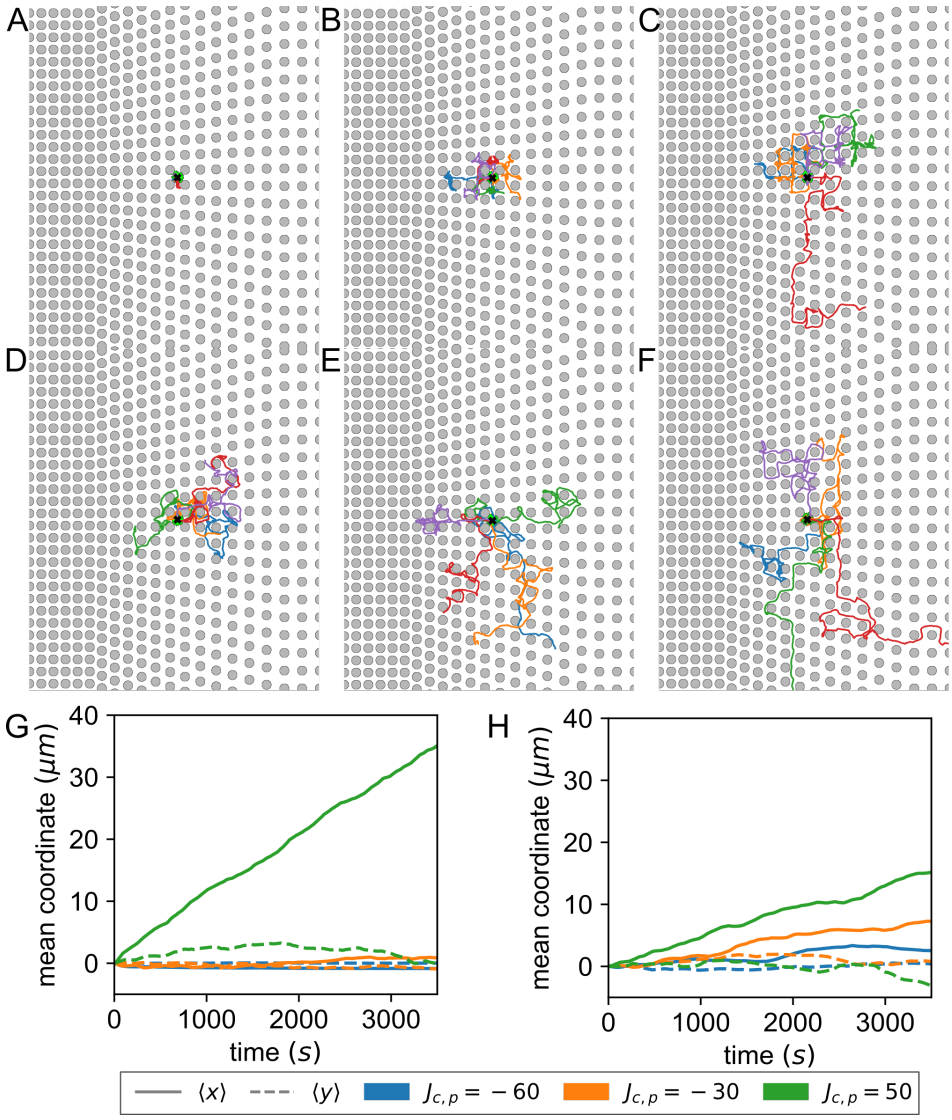

FIGURE 4.7: **Trajectories of starved simulated cells and mean x and y coordinates over time for different pillar adhesion energy $J_{\text{cell,pillar}}$.** *Top row* active reorientation model example trajectories: **A)** $J_{\text{cell,pillar}} = -60$, **B)** $J_{\text{cell,pillar}} = -30$, **C)** $J_{\text{cell,pillar}} = 50$. *Middle row* passive reorientation model example trajectories: **D)** $J_{\text{cell,pillar}} = -60$, **E)** $J_{\text{cell,pillar}} = -30$, **F)** $J_{\text{cell,pillar}} = 50$. Starting location is marked with a black cross and the depiction of a cell. Each trajectory has its own color. *Bottom row* mean x and y coordinates over time of a 1000 independent simulations. **G)** Active reorientation model. **H)** Passive reorientation model.

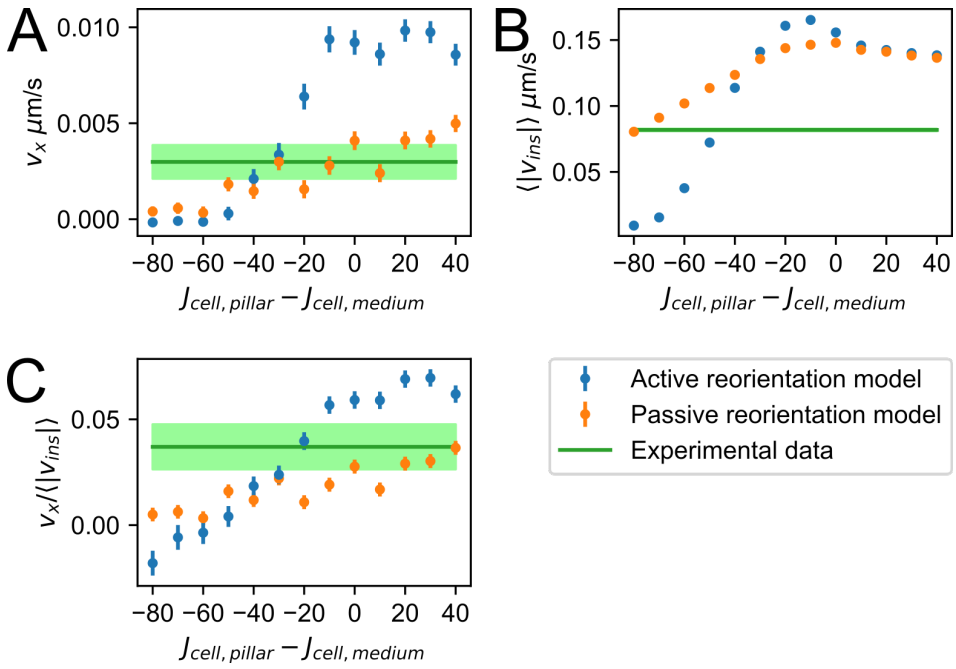

FIGURE 4.8: **Topotactic drift and instantaneous speed of starved parameter set against adhesion preference $J_{\mathbf{cell,pillar}} - J_{\mathbf{cell,medium}}$.** For all points $J_{\text{cell, medium}} = 20$. Each data point represent the average of a 1000 simulations, error bars indicate 97.5% confidence interval. Line with shaded area represents the experimental data with 97.5% confidence interval. **A)** Topotactic drift v_x. **B)** Instantaneous speed $\langle|v_{ins}|\rangle$. **C)** Relative topotactic drift $v_x/\langle|v_{ins}|\rangle$.

Overall, we conclude that adhesion energy between cell and pillar can indeed lower the velocity of cells. However, the drop in speed is paired with a drop in displacement as well, and the values at which it occurs at are not in agreement for when v_x coincides with the experimental v_x.

4.2.7 Effective persistence decreases sooner in active reorientation model than in passive reorientation model

In Schakenraad et al. [75], topotaxis was explained as a change in effective persistence length $l_{\text{eff}} = v_{0,\text{eff}} \cdot \tau_{\text{eff}}$ and effective diffusion D_{eff} due to the presence of pillars, which they verified by simulating a regular grid for a range of different pillar distances d. To further delve into the difference in topotaxis efficiency between the active and passive reorientation model, we also looked into the effective persistence length and effective diffusion over a range of pillar distances. We obtain τ_{eff} by fitting the MSD with Fürth's equation with translational diffusion (Eq. 4.10, see Methods section) and D_{eff} by fitting the MSD at larger time lags with a straight line, similarly to how we obtained them for fitting the empty field data, and obtain $v_{0,\text{eff}}$ by computing $\langle |v_{ins}| \rangle$.

Figure 4.9 shows the effective parameters of the fitted random persistent walk of both models using the starved parameter setting. The two persistence methods react differently to the presence of pillars in regular grids. The effective diffusion coefficient, persistence time and persistence length show a similar trend (Fig. 4.9ABD): they increase as pillar distance increases and saturate to the corresponding values of the empty field measurements. However, this happens more rapidly for the passive reorientation model than for the active reorientation model. The difference in persistence length is mostly due to the difference in persistence times between the two models, as the differences in velocity are minor (Fig. 4.9C). As τ_{eff} is the only measure we determine by fitting Eq. 4.10, we checked whether Eq. 4.10 fits the MSD well. Except for both models on $d = 13.1\mu m$ and the active reorientation model with $d = 14.7\mu m$, the fits seem good. For $d = 13.1\mu m$, the active reorientation model's MSD indicated subdiffusive behaviour: i.e. the cells get stuck between the pillars, whereas the passive reorientation model's MSD did show long term diffusive behaviour but its fit was off for the shorter time scale. The fit for the active reorientation model at $d = 14.7\mu m$ seems to overestimate the persistence time. Nonetheless, at larger d the fits are good and τ_{eff} is decreased more in the active reorientation model. So although the two models behave similarly in an empty field, their behaviour in regular pillar grids is very different, and the persistence of the active reorientation model is more affected by the presence of pillars.

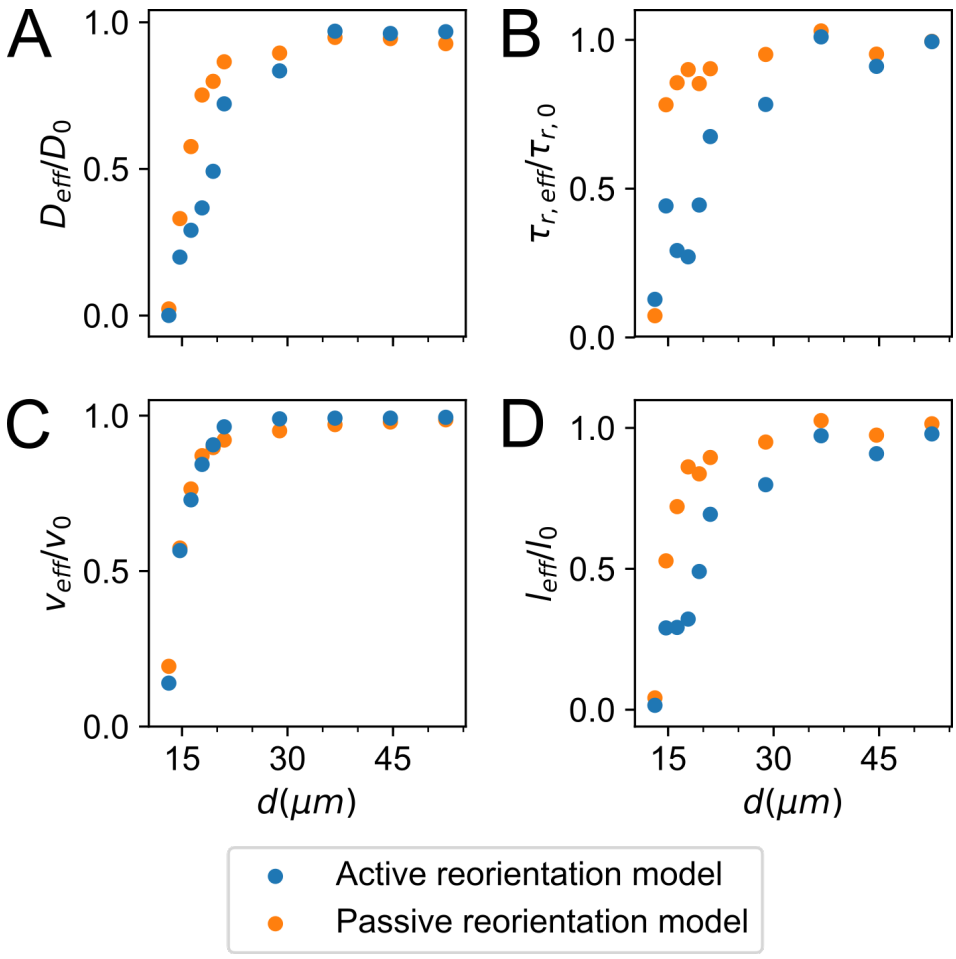

FIGURE 4.9: **Normalized effective parameters of the persistent random walk in regular pillar lattices for the active and passive reorientation model with the starved parameter settings. A)** Effective diffusion coefficient D_{eff} normalized by the diffusion coefficient of starved simulations on an empty field as a function of the distance d between pillar centers. **B)** Effective persistence time τ_{eff} normalized by the persistence time of starved simulations on an empty field as a function of d. **C)** Effective instantaneous velocity v_{eff} normalized by the instantaneous velocity of starved simulations on an empty field as a function of d. **D)** Effective persistence length $l_{\text{eff}} = v_{\text{eff}}\tau_{\text{eff}}$ normalized by the persistence length of starved simulations on an empty field as a function of d.

4.2.8 Model predicts small topotactic drift for vegetative cell topotaxis, but independent of persistent mode

Although no experimental data is available on topotaxis in vegetative cells in these pillar gradients, we are still interested in whether vegetative cells could perform topotaxis. The largest difference in motility between starved and vegetative cells is the lower speed and lower persistence time in the vegetative cells (Table 4.1), and hence, a lower persistence length of about 2.3 µm. The minimum distance between pillars in our pillar grids is significantly larger than that. Hence, we would not expect the persistence of the cell to be altered much in the presence of pillars and therefore deem it unlikely that persistence driven topotaxis contributes much to topotaxis of vegetative cells.

We use our model to predict whether vegetative cells topotax or not. We can see the lower motility of vegetative cells reflected in the example trajectories of our simulated vegetative cells (Fig. 4.10) where cells only move in the order of magnitude of 1-3 cell lengths on the same time scale as in Figs. 4.5,4.7. Still, there is a visible increase in the mean x coordinate but not mean y coordinate (Fig. 4.10), so vegetative *Dictyostelium* cells can likely perform topotaxis as well.

With the lowered displacement of vegetative cells, also v_x is an order of magnitude smaller than that of starved cells (Fig. 4.12A). For $s = 0.01$, the topotactic drift does hardly exceed the drift in the y-direction, (student's t-test $p = 0.01$ for actively reorienting cells, $p = 0.67$ for passively reorienting cells) which indicate how small the topotaxis effect is in a shallow gradient. As the v_x confidence intervals for the starved cell simulations are much smaller compared to those of the experimental starved cells, we expect that it will probably be very hard to measure topotaxis in the experimental system with vegetative cells. The topotactic drift does still increase for higher s , similar to the starved cells. Unlike for the starved cells, the different persistence methods results in similar v_x (Fig. 4.12A) and similar v_{ins} (Fig. 4.12B) and hence also in similar relative topotactic velocity (Fig. 4.12C) for the vegetative cell parameter set. Interestingly, the relative topotactic drift of vegetative cells lies in the range of those of starved vector persistent cells (Fig. 4.6C).

As we did see topotaxis occurring in the vegetative cells, we also looked into the behaviour of these cells in regular grids. We again checked their effective diffusion, effective instantaneous velocity, effective persistence time and effective diffusion length as a function of distance between pillar centres, similar to previously done for the starved cells. Again, we obtained τ_{eff} by fitting Eq. 4.10 to the MSD. For the vegetative cells, we observed

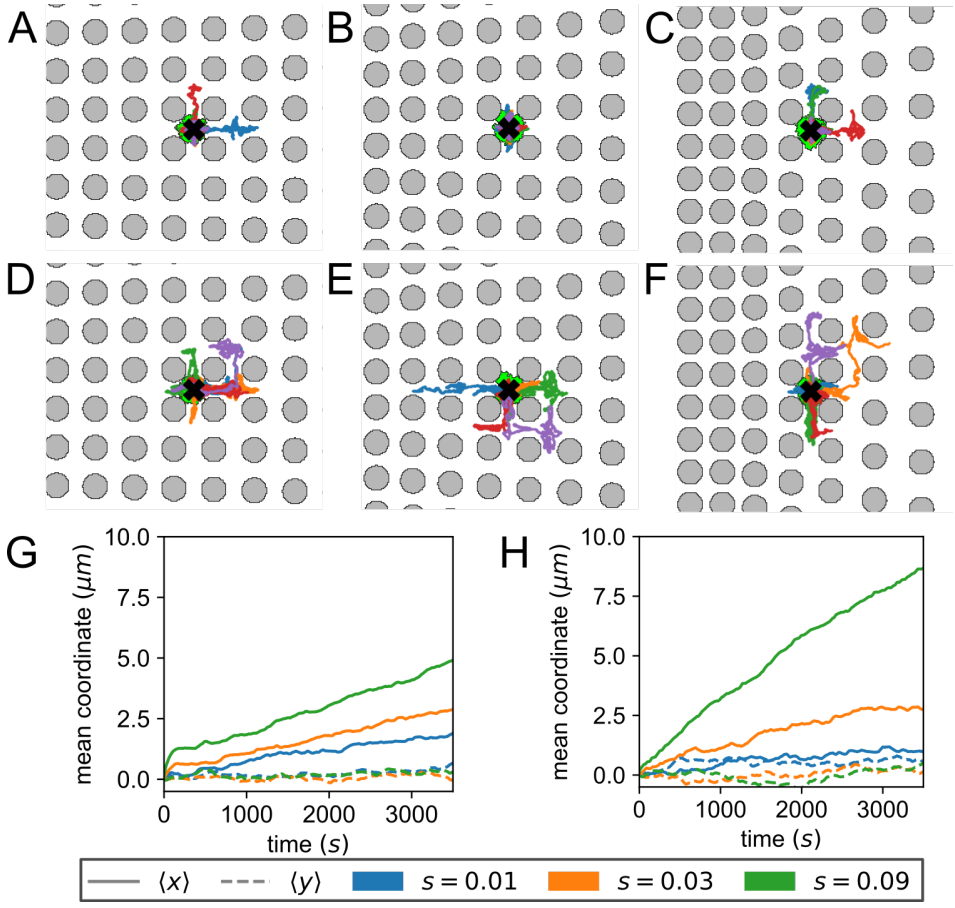

FIGURE 4.10: **Trajectories of vegetative simulated cells and means of x and y coordinates over time for different gradient steepness s.** *Top row*: active reorientation model trajectory examples: **A)** $s = 0.01$, **B)** $s = 0.03$, **C)** $s = 0.09$. *Middle row*: passive reorientation model. Trajectory examples: **D)** $s = 0.01$, **E)** $s = 0.03$, **F)** $s = 0.09$. For the trajectory plots: starting location is marked with a black cross and the depiction of a cell. Each trajectory has its own color. *Bottom row* mean x and y coordinates of 1000 independent simulations. **G**) Active reorientation model. **H**) Passive reorientation model.

that for the active reorientation model, Eq. 4.10 is not a good descriptor of the MSD for low pillar distance $d = 13.1\mu m$ to $d = 16.2\mu m$. Hence, we only show the results in Figure 4.11 for $d > 16.2\mu m$. The effective parameters are more similar between the persistence methods than observed for the starved parameter set (Fig. 4.9). Only on the smallest displayed pillar distances d, we see that the effective persistence time of the active reorientation model is more affected than of the passive reorientation model. Compared to the differences between the persistence methods for the starved cells, this difference here is smaller in both relative and absolute manner. Overall, these effective parameters do not indicate a clear difference between the persistence methods for vegetative cells.

4.3 Discussion

In this paper we have measured topotaxis by *Dictyostelium discoideum* cells in a pillar gradient as well as simulated topotaxis in a similar grid using the Cellular Potts model. Persistent *Dictyostelium* motion was modelled through two distinct persistence modules in our model: the Act model, and a vector-based persistence of which the direction changes over time. We fitted our model parameters to match *Dictyostelium* motion on an empty field before we simulated topotaxis in a pillar grid.

For starved cells, we saw that, for shallow gradients, increasing the gradient steepness increases topotaxis, both in the experiments and the simulations. This is in agreement with [75]. The topotactic velocity of both persistence methods follows a linear trend in gradient steepness, but the actively reorienting cells are more efficient in topotaxis than the passively reorienting cells, regardless of having similar instantaneous velocity.

We further looked into the cause of difference between the active and passive reorientation model and found that the effective persistence length on regular pillar grids is more affected by short pillar distances in the active model than in the passive model. The difference in effective persistence length arises from the difference in persistence time. We conclude that the active reorientation model is more likely to change orientation upon collision than the passive reorientation model, explaining the lower effective persistence time and effective persistence length.

Aside from the difference between our two models, the instantaneous velocity is a major point of difference between the experimental and simulation results. By lowering the adhesion energy between cell and pillar, we were able to lower the instantaneous velocity of the simulated cells. However, this also resulted in reduced displacement, to the point that

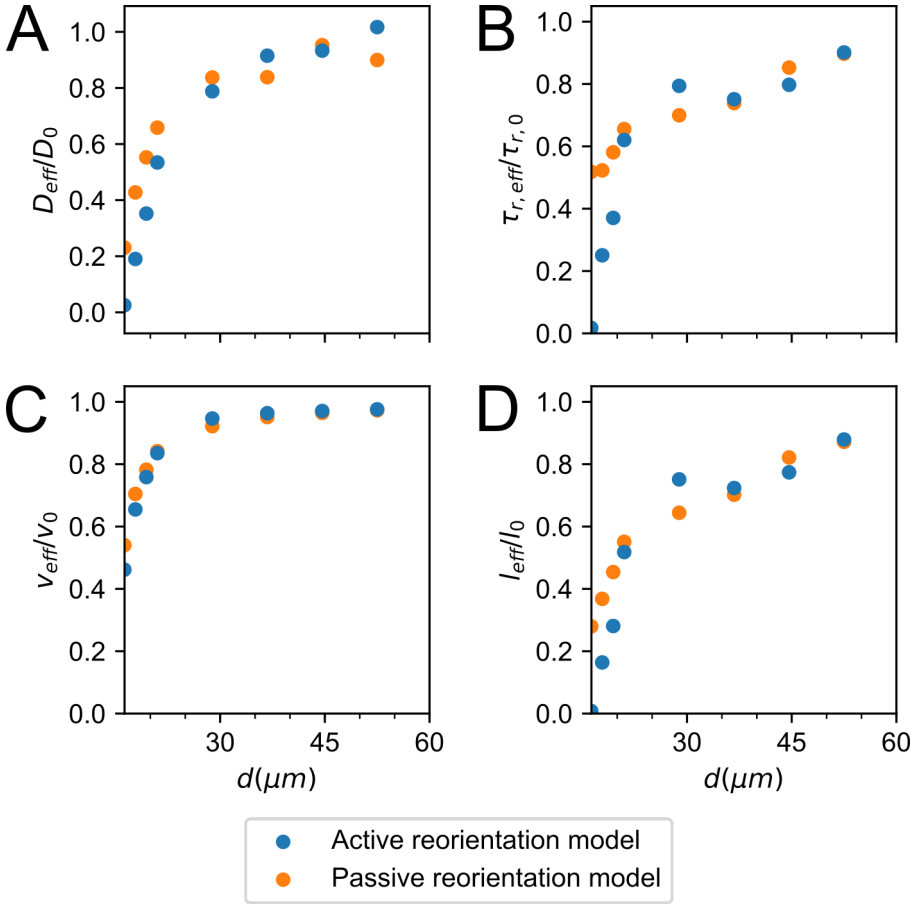

FIGURE 4.11: **Normalized effective parameters of the persistent random walk in regular pillar lattices for the active and passive reorientation model with the vegetative parameter settings. A)** Effective diffusion coefficient D_{eff} normalized by the diffusion coefficient of vegetative simulations on an empty field as a function of the distance d between pillar centers. **B)** Effective persistence time τ_{eff} normalized by the persistence time of vegetative simulations on an empty field as a function of d. **C)** Effective instantaneous velocity v_{eff} normalized by the instantaneous velocity of vegetative simulations on an empty field as a function of d. **D)** Effective persistence length $l_{\text{eff}} = v_{\text{eff}}\tau_{\text{eff}}$ normalized by the persistence length of vegetative simulations on an empty field as a function of d.

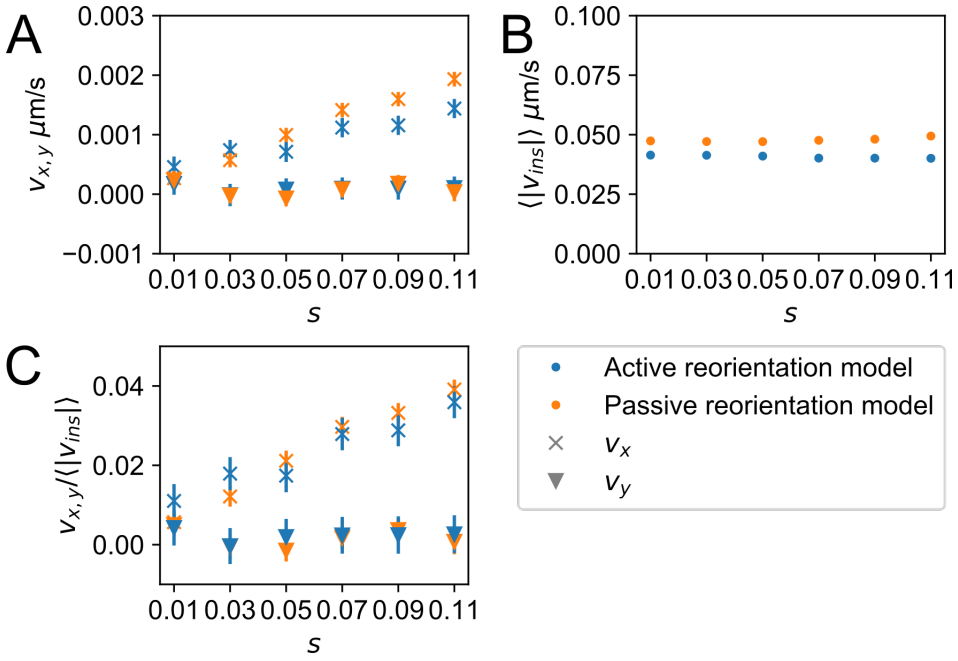

FIGURE 4.12: **Migratory drifts and instantaneous speed of vegetative parameter set against gradient steepness** s**.** Each data point represent the average of a 1000 simulations. Error bars indicate 97.5% CI. **A)** Migratory drifts v_x (lighter colors) and v_y (darker colors). **B)** Instantaneous speed $\langle|v_{ins}|\rangle$. **C)** Relative drifts $v_x/\langle|v_{ins}|\rangle$ (lighter colors) and $v_y/\langle|v_{ins}|\rangle$ (darker colors).

cells are sticking to the pillars. Hence, pillar adhesivity is unlikely the only mechanism to explain the velocity difference between experiment and simulation.

For the vegetative simulations, our model predicts that cells do undergo topotaxis distinct from directional noise, albeit an order of magnitude smaller than the starved cells, with the exception of the shallowest gradient. Also, both persistence modes resulted in similar outcomes, suggesting that there is a difference in topotaxis by quick and persistent cells and slower, less persistent cells.

4.3.1 Topotaxis and the changing effective persistence length

The physical principle underlying topotaxis presented in Schakenraad et al. [75] states that the change in effective persistence length caused by the pillar grid causes ABP to turn towards regions where they display higher effective persistent length. This idea is similar to that of how durotaxis, i.e. motion up a stiffness gradient, arises [193, 146].

When we compare the efficiency in topotaxis of both the *D. discoideum* cells and the CPM simulations to the ABP simulations, both the cells' and CPM simulations' relative topotactic velocities well exceed the 1% topotactic velocity of ABPs, the passive reorientation model at the shallowest gradient excluded. For the models, we can explain this difference by the difference in effective persistence length in a pillar grid. In our model, the effective persistence length is decreased more at small pillar distances than the ABP model. As this is true for both reorientation models, we conclude that this is an effect of the dynamic volume of our simulated cells.

Furthermore, when comparing the persistence length of the active and passive reorientation models, the difference in persistence length between the two models could explain the difference in relative topotaxis. Interesting to note here is that the change in persistence length can be ascribed to the change in persistence time and not change in velocity. We can interpret this as actively reorienting cells changing direction more drastically upon colliding with a pillar. We hypothesize that, for the active reorientation model, the new direction after collision is more uniformly distributed along the directions not pointing towards the pillar center, i.e. contact inhibition of locomotion, whereas reorientation direction for the passive reorientation model is more skewed towards the previous direction. This reorientation effect can likely be exaggerated by looking at concave obstacle shapes.

In this perspective, we can also look at the vegetative simulations. As the persistence length and persistence time for vegetative cells is very short,

the differences in how the models reorient upon collision becomes negligible. We also observed hardly any difference in the effective parameters within regular grids between the two persistence methods, except for small distances between pillars. The lack of difference in these parameters is likely why the resulting topotaxis is so similar between the models.

The reorientation of cells upon obstacle collision has also been subject of other studies [197, 198, 199]. In an experiment with fish keratocytes, actin flow was disturbed upon collision with an obstacle, making the keratocyte change direction [197]. Modelling studies also indicate that intercellular molecular dynamics are important in cell reorientation upon collision. In Nishimura et al. [198] the change in actin retrograde flow plays an important role in the formation of a new protrusion after collision with a wall, allowing the cell to move away from the wall. In Campbell et al. [199] many different cell behaviours after collision were observed in a immersive-boundary method with reaction-diffusion equations on the cell surface. They observed 1) 'freezing' when the cell did not have new pseudopods for a short while after collision, 2) 'doubling back' when the cell return in the direction it came from and 3) 'tug of war' were the new pseudopods competed for leading the cell's new direction.

4.3.2 Dictyostelium on silicon and *in silico*

We saw a disparity between the instantaneous speed of the *D. discoideum* cells and the simulated cells when they were within the pillar grid. This difference is unlikely to be caused by cells adhering to the pillars. Some other mechanisms could be at play, such as dimensionality, curvotaxis and chemotaxis. We will shortly address each of them.

Dimensionality

Our Cellular Potts model is a 2D model. However, the experimental cells crawled in a 3D pillar grid and hence can use the third dimension while moving around the obstacles. Experimental observation show that *D. discoideum* cells sometimes crawl up a pillar, mainly displacing their center of mass vertically. They can also move through narrower pillar distances than our CPM simulation by spreading their volume vertically. Although vertical displacement is not modeled directly in the CPM, the weight of the area and perimeter constraint can be seen as a measure of 3D flexibility. A possibility would be to extend our models into a 3D CPM, or use other computational methods, such as in [199]. Furthermore, how our results translate to 3D matrix environments is still unclear. As shown in [200], cells

migrate very differently in 1D and 3D matrix environment compared to 2D matrix environments, so translating topotaxis from our experiments to more complex structures is non-trivial.

Curvotaxis

Aside from the dimensionality difference, there is another aspect to the experimental setup. The interpillar distance is slightly curved, as the pillars are broadening at their feet. It has been shown that cells are responsive to substrate curvature on the cell-scale [201, 202, 203], and tend to move towards concave “valleys". The interpillar spaces with concave curvature fit this description, and could alter the speed of *Dictyostelium* cells.

Chemotactic sensing

More guiding principles can be at play. *Dictyostelium discoideum* cells are known to secrete cAMP when starved, but can also degrade cAMP when in high concentrations [204]. This chemical functions as a chemoattractant. Usually, this will lead to multiple cells to find each other and aggregate. In a modeling study it has been shown that these aggregates can avoid obstacles through the perturbations in the chemical field caused by such obstacles [205]. However, not many studies have been done on how this affects single *Dictyostelium* cells and whether they can sense their own secreted cAMP. Nonetheless, multiple studies have shown how chemical sensing of the environment can guide cell movement around large obstacles [206], or through mazes [207]. Self-secreted chemoattractant can also trap cells within containing environments such as dead ends in mazes [208]. The effect of chemical sensing in a field with a high density of obstacles as well as its effect in topotaxis is still open for study.

Concluding, our model is a much closer match to the behaviour of *Dictyostelium discoideum* cells in pillar grid with a distance gradient than the previous, analytical ABP model. The deformable cell volume within our models allows for more efficient topotaxis as it lowers the effective persistence length, especially when pillar distance is close to the cell length. We also showed that how cells interact upon collision plays an important role in the effective persistence length and hence, topotaxis.

4.4 Materials, Methods, and Model

For this study, we have used an experimental setup with live cells and a computational model. Experimental data from cells on a flat surface were

used to set the model parameters. Topotaxis measurements were done in both the experimental as well as the computational setup.

4.4.1 Live cell experiments

Cell culture and experiment preparation

For all migration experiments, Axenic *D. discoideum* (Ax2) with a cytoplasmic green fluorescent protein (GFP) insertion was used (strain HG1694, obtained from Dr. G. Gerisch, MPI for Biochemistry, Germany). Cells were grown at 20 °C in HL5 medium, supplemented with 20 $\mu g ml^{-1}$ gentamicin (Gentamycin solution, Merck, Netherlands) as a selection antibiotic. The cells were cultured in 100 mm petri dishes (100 mm TC-treated culture dish, Corning, USA) and confluency was kept below 70% during culturing. For visualizing actin polymerization, a LimE-GFP in lim0 cell line was used [195]. These cells were cultured similarly, but with two selection antibiotics, 10 $\mu g ml^{-1}$ Gentamycin and 10 $\mu g ml^{-1}$ Blasticidin, necessary to maintain the double mutation (LimE-GFP and Lim0).

In preparation for imaging experiments, cells were harvested by pipet induced flow and collected in a conical tube. To remove the culture medium the cells were centrifuged at 1500 rpm for 3 min. In case of vegetative experiments, resulting cell pellets were thrice washed using non-fluorescent buffer (3.6mM KH_2PO_4, 2.9mM Na_2HPO_4, PH 6.7) and, after resuspension, transferred onto (un)structured polydimethylsiloxane (PDMS) surfaces placed inside an imaging chamber (see Sec. 4.4.1). In case of starved experiments a pulsation procedure was started before imaging instead. Cell pellets were thrice washed with 17 mM K-Na-phosphate buffered saline (PBS, pH 6.0) and placed on a shaker for 1 hour. Then, to induce cAR1 expression, cells were pulsed with 150 nM cyclic adenosine-monophosphate (cAMP, Merck, The Netherlands) applied in 6 minute intervals over 4 hours while shaking. After pulsation, any residual cAMP was removed by centrifugation and resuspension. Cells were left to shake in a conical tube with PBS for another 30 min before being loaded onto PDMS surfaces in imaging chambers. For both experiments cells were left to adhere for 1 hour after insertion into the imaging chamber, leading to a 6-7 hour starvation period. Cell seeding concentrations were kept below $1 \cdot 10^{-4}$ μm^{-2} to limit cell-cell interaction and enable studying migration of individual cells.

Obstacle and flat PDMS surfaces

PDMS (Sylgard 184 Silicon Elastomer Kit, Dow Corning, USA) was mixed 1:10 resulting in a 1.72 MPa stiffness for all surfaces [209]. Flat surfaces were

prepared by spin-coating pre-mixed PDMS onto polished Silicon wafers (Siegert Wafer, Germany) and then baked for 4 hrs at 110 °C. Before spin-coating, wafers were silanized by Trichloro(1H,1H,2H,2H-perfluorooctyl) silane deposition under vacuum (50 mbar) for 1 hour to ensure proper PDMS detachment later. Before use, PDMS was cut, peeled off, and washed with ethanol (70%). For migration experiments PDMS was cast around a 250-500 µm thickness, for limE-GFP imaging, PDMS was cast ultra-thin (<50µm) enabling 100x (WD= 130µm) imaging.

Pillar obstacle fields were prepared using a molding process. The pillar molds were prepared by two-photon direct laser writing (DLW) using the Photonic Professional GT (Nanoscribe, Germany). First, a negative of the topotaxis pillar lattices ($s = 0.01$-0.03, see Section 4.4.2) were designed using Inventor (Autodesk, USA) and, via a stereolithography format (.stl), imported to DeScribe (Nanoscribe, Germany) to prepare for DLW. Then, two-photon crosslinking was performed using the IP-S resin (Nanoscribe, Germany) deposited on a silicon wafer. Different laser powers and scan speeds were chosen for bulk and edges of the structure, 27% and 42% (of 140 mW), 10 and 40 mm/min respectively. To remove excess resin, molds were developed for 45 min in polyglycidylmethacrylate (PGMA). After blow drying with nitrogen, wafers were silanized as described previously. To produce the pillar field casts, PDMS was deposited over the wafer (with mold on top), baked, cut, peeled off, and washed with ethanol (70%).

PDMS inserts were hydrophilicitized by 15 min of UV/Ozone exposure (UVO-42, Jelight Company, U.S.A) and placed inside an imaging slide (0.8 sticky-Slide I Luer, Ibidi, Germany), to be used immediately. Before loading cell suspensions, imaging slides were washed with ethanol and then PBS.

To determine quality of the mold, each pillar field was imaged using a nanoSEM (FEI/Thermo Fisher, The Netherlands) scanning electron microscope (SEM). Samples were imaged at 10kV, with a spot size of 4.0. Before imaging, PDMS structures were coated with 2-8 nm Pt/Pa using a plasma magnetron sputter coater (208HR, Cressington, Watford, UK) to enhance conductance.

Live-cell imaging and tracking

Cells were imaged every 8-10 seconds for experiments on flat PDMS and every 20 seconds for topotaxis assays. Measurements lasted for 1-3 hours and were performed with either 10x or 20x air objectives (Plan Fluor, Nikon) on a Nikon Eclipse Ti microscope equipped with a confocal spinning disk unit operated at 10,000 rpm (Yokogawa). The cytoplasmic GFP was excited at 488nm by a solid-state diode laser (Coherent, U.S.A.) supported in an

Agilent MLC4 unit (Agilent Technologies, U.S.A.), at reduced intensity (25% of 2.4mW) controlled by an Acousto-Optic Tunable Filter. Emission was filtered by a quad-band fluorescence filter (TR-F440-521-607-700, IDEX LLC, Rochester, New York, U.S.A.). Images were captured using an exposure time of 200ms by an Andor iXon Ultra 897 High Speed EM-CCD camera (Andor Technology, U.K.). Images of higher magnification were produced with the same setup but using different objectives: Figure 4.4e with 40x air (PlanFluor, Nikon), limE-GFP Figures 4.4d and 4.3a with 60x water (Plan Apo VC, Nikon) and 4.1c and 4.2a with 100x oil (CFI plan Apo, Nikon).

Image tracking was performed using ImageJ (http://imagej.nih.gov/ij/). Microscopy time-lapse images were contrast and brightness adjusted, and ran through a Gaussian filter ($\sigma = 2$) to enable optimal cell body recognition. The ImageJ plugin CellEvaluator was used to determine the x, y-coordinates of the center-of-mass of each cell body in each frame [210]. By linking all these x, y-positions together, cell trajectories were obtained.

Empirical measurement of cell area

Fluorescence microscopy of cell migration experiments on flat PDMS were used to fit the cell surface area (A_σ) parameter in the CPM. Frames used for area analysis were chosen sufficiently far apart ($f^{-1} = \delta t = 200$ s) to avoid correlations. The two-dimensional projection of the cell body was determined using Sobel edge detection, applied to cytoplasmic GFP images obtained using the 20x air objective (0.657 µm/pix). Brightness and contrast were adjusted to rescale pixel intensities (i.e. only use the range of 16-Bit intensities of GFP signal detected). Image analysis was performed using Matlab, and the Image Processing Toolbox (Matlab v2019a, MathWorks, U.S.A.) in particular. First, edges were detected (Sobel) using an appropriate threshold, then the resulting binary edge-image was dilated, holes were filled, borders cleared and the image eroded (equal to the initial dilation). Then all groups of non-zero, adjacent pixels forming a cell were identified and properties (using *regionprops*) like area extracted.

Amoeboid movement on flat and pillar surfaces

We analysed cell migration trajectories, measured on flat and pillar PDMS, with an in-house Matlab code (version 2019b, The Mathworks, U.S.A.). The empirical instantaneous velocities (v_{inst}), persistence times and diffusion constants of cell movement measured on flat PDMS were used to fit the CPM model for both cell types. These were calculated from the cell trajectories obtained in combination with the known frame rate ($f^{-1} = \delta t = 20$

s) between images. Dying or otherwise immotile cells (see [74]) and insufficiently long trajectories (flat $N < 100$, topotaxis $N < 30$) were discarded for analysis. N was chosen higher for the flat data set, to prevent noise in mean-squared displacement (MSD) values at long-lag times.

The displacement (r) of the cell between frames is given by $\bar{r}(t) = \bar{R}(t + \delta t) - \bar{R}(t)$, where $\bar{R}(t)$ are the vectors described by the x, y-coordinates of the cell center in each image. Then, the instantaneous velocity ($v(t)$) and MSD were calculated for each trajectory by,

$$v(t) = \frac{|\bar{r}(t)|}{\delta t} \text{ and } \langle \bar{r}(\tau)^2 \rangle = \frac{1}{N-k} \sum_{i=1}^{N-k} (\bar{R}(t_i + \tau) - \bar{R}(t_i))^2. \tag{4.1}$$

Here, $\tau = k\delta t$ is the lag time, N the number of points in a trajectory, and k the frame number ($k = 1, 2, \ldots N - 1$). The MSDs were averaged over all trajectories, and subsequently fit to Fürths formula for persistent random motion. From this fit the characteristic persistence times (τ_r) and effective diffusion constants (D_{eff}) for both vegetative and starved *D. discoideum* cells moving on flat PDMS were extracted and used to fit the CPM.

For flat and topotaxis assays, migratory drift ($v_{x,y}$) was calculated by averaging over all displacements of all trajectories,

$$\langle v_{x,y} \rangle = \frac{1}{n-1} \sum_{i=1}^{n-1} (\bar{R}(t_i + \delta t) - \bar{R}(t_i)) \tag{4.2}$$

where n is the total number of displacements measured.

4.4.2 Model

The model is based on the 2D Cellular Potts model and hence models cells as flexible and dynamically shaped objects in two dimensions. Cell persistence is obtained using two methods: one phenomenologically models actin dynamics, the other has a set preferential direction for the cell to move in that changes over time. We fit the parameters of these methods such that the simulated cells perform the same persistent random walk as measured experimentally in the starved and vegetative *Dictyostelium discoideum* cells on the flat PDMS surfaces. After fitting the parameters, we use the found parameter settings in our simulations with a pillar grid. The grid either contains a gradient in pillar spacing in the x-direction, or is regularly spaced. In the gradient grid, we measure the average step size in the x-direction and speed of the cell. For the regular grids, we determine the effective

persistence time, persistence length, speed and diffusion coefficient. In each of our simulations, we simulate a single cell.

Cellular Potts model of persistently moving cells

The model of cell movement is based upon the Cellular Potts model (CPM) [68] with either of two extensions for modeling persistent cell movement (see Section 4.4.2). The CPM represent cells on a regular square lattice $\Lambda \subset \mathbb{Z}^2$. Each lattice site, $\vec{x} \in \Lambda$, is associated with a spin value $\sigma(\vec{x}) \in \{-2, 0, 1\}$, or *cell ID* that uniquely identifies the lattice site with the cell ($\sigma = 1$), the medium ($\sigma = 0$), or a pillar ($\sigma = -2$). The cell is represented as a collection of lattice sites marked with $\sigma = 1$.

Cell motion is modelled by updating the grid through random copy attempts. In a copy attempt a lattice site x is selected randomly, as well as one of its neighbours y. If $\sigma(x) \neq \sigma(y)$, the copy attempt can change the energy of the system. Whether a copy attempt is accepted depends on the energy change associated with it. The energy of the cell is described by the Hamiltonian $\mathcal{H}$, that contains cell-medium and cell-pillar interactions and two cell constraints: the cell area and the cell perimeter [70].

$$\mathcal{H} = \sum_{u,v} J_{\sigma_u,\sigma_v}(1 - \delta_{\sigma_u,\sigma_v}) + \lambda_{\text{area}}(a_\sigma - A_\sigma)^2 + \lambda_{\text{perimeter}}(p_\sigma - P_\sigma)^2 \quad (4.3)$$

The first term in the Hamiltonian describes the adhesion energy of the cell. Here, J_{σ_u,σ_v} describes the interaction energy between two neighbouring lattice sites u, v of types $\sigma(u), \sigma(v)$. As $J_{\text{pillar,medium}} = 0$, we only take the adhesion energy between cell and medium or cell and pillar into account. The second term describes the area constraint and penalizes deviation of the cell area a_σ from its target area A_σ. The third term is the perimeter constraint and penalizes deviation in cell perimeter p_σ from the target perimeter P_σ. The λ's indicate the weight of both constraints.

The probability of a successful copy attempt depends on the change in Hamiltonian:

$$P(\Delta\mathcal{H}_{\mathbf{x}\to\mathbf{y}}) = \begin{cases} 1 & \text{if } \Delta\mathcal{H} < 0 \\ e^{-(\Delta\mathcal{H}/T)} & \text{if } \Delta\mathcal{H} \geq 0 \end{cases},$$

with T denoting "the temperature", a term that allows for noise, as cells are able to use energy to do energetically unfavourable moves by energy expenditure. To keep track of time, the model time is expressed in Monte Carlo steps (MCS). Within a single MCS, the expectation is that each lattice site has been updated once. Since we only model a single cell in a large

field, many lattice site neighbouring pairs will not lead to cell movement. To speed up simulations, we use a rejection-free algorithm ignoring such unfruitful copy attempts.

Pillars

The pillars in our model have their own $\sigma = -2$, as not to be confused with the σs of the medium or cells. Updates involving a pillar are handled differently from other updates. As pillars are static, we do not allow a copy attempt into a pillar site. However, we allow for copy attempts from a pillar site into a cell. Although, in this case, we do not copy $\sigma(pillar)$ into the site, but $\sigma(medium)$. This allows the cells to retract from the pillars and can be seen as medium flowing back in from the third dimension which we do not model explicitly. The interaction energy $J_{\text{cell, pillar}}$ can be adjusted to represent highly adhesive or slightly repulsive pillar surfaces. In this work, our base value is set to $J_{\text{cell,pillar}} = J_{\text{cell,medium}}$, such that pillar adhesion is neutral in respect to adhesion to the medium, but we also vary $J_{cell,pillar}$ to see the effect of adhesion.

We model two different pillar grids: a regularly spaced pillar grid and a pillar grid with a gradient. The regularly spaced grids are defined by the distance between pillar centers d and the pillar radius R. We set $R = 10px \approx 5.25\mu m$ in our simulations. The pillar grid with gradient consist of three different parts: a regularly spaced part on the left of the field, a part with a gradient in pillar distance in the middle and another regularly spaced part on the right. The gradient of pillar in the middle is defined by the following set of pillar centers P,

$$P = \left\{ \vec{x} \in \mathbb{R}^2 \;\middle|\; \begin{array}{l} x_1 = \frac{d}{1-e^{-s}}(e^{sn} - 1) + \frac{d}{2} \text{ and} \\ x_2 = d\left(m + \frac{1}{2}\right) e^{sn}, \text{ with } n, m \in \mathbb{Z} \end{array} \right\}, \tag{4.4}$$

where d is the distance between pillar centers at the origin $(0, 0)$, the center of the field. We used $d = 32px \approx 16.8\mu m$ in our simulations and $d = 16.8\mu m$ in the experimental setup. The parameter s defines the steepness of the gradient. A lattice site $\vec{x}$ is assigned to a pillar if it is within a distance R from one of the pillar centers, $\vec{p} \in P$. Hence the set of pillar lattice sites becomes,

$$\{\vec{x} \in \Lambda | (\exists \vec{p} \in P)[|\vec{x} - \vec{p}| < R]\} \tag{4.5}$$

with P the set of lattice centers (Eq. 4.4), and R the pillar radius. Again, we set $R = 10px \approx 5.25\mu m$ in our simulations. For the experimental setup $R = 5\mu m$.

This gives a gradient in the horizontal axis. However, to limit the gaps between pillars to get too small or too big, we have the two regularly spaced grids at the left and right of the gradient part of the grid. The pillar spacing of those two parts is set to $d_{min} = 2R + 6px \approx 13.65\mu m$ on the left and $d_{max} = 2d - d_{min}px \approx 19.95\mu m$ on the right in our simulations, and in our experimental setup $d_{min} = 13.63\mu m$ and $d_{max} = 19.93$. See also Table 4.3 for an overview of all grid measurements.

Persistent random walker

Our Hamiltonian on its own does not lead to persistent cell motion. In order to model persistent cells, we use two different extensions of the Cellular Potts model. First, we use the Act-extension [73], which models internal cell skeleton rearrangements and is also capable of describing persistent cell motion. Secondly, there is the vector-based persistence, which inherits most of the properties of the persistence model by Schakenraad et al. [75].

Act-extension - Active reorientation The Act-extension for the Cellular Potts model adds an extra layer to this model that resembles the assembly of actin machinery [73]. Each lattice site has an extra value, called the Act-value, which can range from 0 to $\max_{Act}$, a parameter value. The Act-value outside the cell is always 0, and can vary inside the cell. If the cell has recently made an extension, the site of extension will get the Act-value of $\max_{Act}$. Each Monte-Carlo step, the Act-values will be decreased by 1, until they become 0.

The Act-values play a role in the change in Hamiltonian. If there is a copy attempt extending a lattice site $\vec{c}$ from the cell into a lattice site $\vec{m}$ containing medium, then we look at the geometric mean of the Act-levels in $\mathrm{NB}(\vec{c})$, the Moore neighbours of $\vec{c}$ that are within the cell, such that:

$$\Delta\mathcal{H}_{Act}(\vec{c} \to \vec{m}) = \frac{\lambda_{Act}}{\max_{Act}} \sqrt[|\mathrm{NB}(\vec{c})|]{\prod_{y \in \mathrm{NB}(\vec{c})} Act(y)}. \tag{4.6}$$

Otherwise, if there is an attempt of a cell retracting, then the sign changes, so $\Delta\mathcal{H}_{Act}(\vec{m} \to \vec{c}) = -\Delta\mathcal{H}_{Act}(\vec{c} \to \vec{m})$. As a consequence, cell areas with high Act levels are more likely to extend outwards of the cells and less likely to retract. This simulates the polarized actin structure of a cell in a phenomenological way. The two parameters λ_{Act} and $\max_{Act}$ can be tuned to obtain different cell motilities.

Vector-based persistence - Passive reorientation The vector-based persistence is a hybrid method between [72] and [75]. First of all, the cell has a direction indicated by θ. Cell movement along this direction is favoured. For each copy attempt extending the cell, the angle α between the displacement caused by that move and θ is computed, and coupled to the Hamiltonian as by [72]:

$$\Delta\mathcal{H}_{\text{persistence}} = -\lambda_{\text{persistence}} \cdot \cos(\alpha). \tag{4.7}$$

$\Delta\mathcal{H}_{\text{persistence}}$ is added to the general $\Delta\mathcal{H}$. For the updating of θ, we deviate from [72], and use the differential equation, the same as in [75].

$$\frac{d\theta}{dt} = \sqrt{\frac{2}{\tau}}\xi(t). \tag{4.8}$$

Here τ stands for the persistence time, and $\xi(t)$ is a stochastic white noise term, modelled by a Gaussian distribution with mean 0 and variance $\sigma^2 = 2\frac{\Delta t}{\tau}$. The term Δt couples the time of equation 4.8 to the MCS, and we choose $\Delta t = 0.1\tau$. At initialization the cell is assigned a θ from a uniform random distribution. We update θ each MCS. We can tune the cell motility of this model extension through the parameters τ and $\lambda_{\text{persistence}}$.

Empty field fitting

In order to quantitatively compare the topotaxis of simulated cells to *Dictyostelium discoideum* cells, we tried to find parameters such that the actively reorienting and passively reorienting cells behave similarly to the starved and vegetative *D. discoideum* cells on a surface without any pillars (Figs. 4.1 and 4.2). We only changed λ_{Act} and $\max_{Act}$, and $\lambda_{\text{persistence}}$ and τ freely.

The values we fitted our cells to are the surface area, instantaneous speed, effective diffusion coefficient and persistence time. The surface area and speed were used to determine the length and time scale of the CPM, whereas the effective diffusion coefficient and persistence time were the objective of our fit. We fitted for starved and vegetative *D. discoideum*. Starved cells on an empty surface displayed a persistent random walk (Fig. 4.1, Table 4.1). Vegetative cells had a larger area and were less motile (Fig. 4.2, Table 4.1)

Determining model persistence time and diffusion coefficient For determining the persistence time in our models, we first have computed the mean squared displacement of 1000 simulated cell tracks from 120 MCS

onwards:

$$\langle r(t)^2 \rangle = \frac{1}{1000} \sum_{i=1}^{1000} (R(120+t) - R(120))^2 \tag{4.9}$$

We then fitted to $\langle r(t)^2 \rangle$ the formula

$$MSD(t) = 4D_T t + 2v_0^2 \tau_r t - 2v_0^2 \tau_r^2 (1 - e^{-t\tau_r}), \tag{4.10}$$

which describes the active Brownian motion with translational noise [159]. Here τ_r is the persistence time, v_0 the constant speed, and D_T is the translational diffusion caused by thermally induced fluctuation, which is inherent in the CPM. The corresponding effective diffusion constant is described by $D_{\text{eff}} = D_T + \frac{1}{2} v_0^2 \tau_r$. However, we decided to obtain D_{eff} independently from Eq. 4.10 by fitting a line through the square displacements over time starting from $t = 2000$ MCS and divide its slope by 4.

Scoring the fit For scoring the fit we used a weighted least squares objective. We used a hillclimbing algorithm with multiple restarts to obtain a shortlist of possible parameter values. The best fifteen parameter sets were then scored ten more times to obtain the best parameter set. The resulting effective diffusion coefficient and persistence time are shown in Table 4.1. The fits for starved cells are better than the fits for vegetative cells, most likely due to the discretization of the parameter space. The optimal parameters are shown in Table 4.2.

Measuring model topotaxis

To measure topotactic drift, we have run multiple simulations for different values of s, the parameter indicating the steepness of the pillar gradient. For each parameter value, we did 1000 simulations. To measure topotaxis we computed the mean velocity in the x-direction at $20s$ intervals for all cell tracks while the cell was in the gradient part of the pillar grid. This gives our migratory drift v_x.

Acknowledgements

We thank SURFsara for the support and computing time in using the Lisa cluster computer. J.A.J.W and D.H acknowledge the Fraunhofer Society for the Fraunhofer Attract grant “3DNanoCell” for partly funding this work and thank Dr. G unther Gerisch (MPI forBiochemistry,Martinsried,

Germany) for providing axenic *D. discoideum (Ax2)* with both free GFP and limGFP in lim0 insertion.